Developmental Cell
Article

IFT27 Links the BBSome to IFT for Maintenance of the Ciliary Signaling Compartment

Thibaut Eguether,[1] Jovenal T. San Agustin,[1] Brian T. Keady,[1] Julie A. Jonassen,[2] Yinwen Liang,[1,4] Richard Francis,[3] Kimimasa Tobita,[3] Colin A. Johnson,[5] Zakia A. Abdelhamed,[5] Cecilia W. Lo,[3] and Gregory J. Pazour[1,*]
[1]Program in Molecular Medicine, University of Massachusetts Medical School, Biotech II, Suite 213, 373 Plantation Street, Worcester, MA 01605, USA
[2]Department of Microbiology and Physiological Systems, University of Massachusetts Medical School, 55 Lake Avenue North, Worcester, MA 01655, USA
[3]Department of Developmental Biology, University of Pittsburgh, 8111 Rangos Research Center, 530 45th Street, Pittsburgh, PA 15201, USA
[4]School of Life Sciences, Tsinghua University, Renhuan Lou 413, #1 Qinghuayuan, Haidian District, Beijing 100084, China
[5]Section of Ophthalmology and Neurosciences, Wellcome Trust Brenner Building, Leeds Institute of Molecular Medicine, University of Leeds, St. James's University Hospital, Beckett Street, Leeds LS9 7TF, UK
*Correspondence: gregory.pazour@umassmed.edu
http://dx.doi.org/10.1016/j.devcel.2014.09.011

SUMMARY

Vertebrate hedgehog signaling is coordinated by the differential localization of the receptors patched-1 and Smoothened in the primary cilium. Cilia assembly is mediated by intraflagellar transport (IFT), and cilia defects disrupt hedgehog signaling, causing many structural birth defects. We generated *Ift25* and *Ift27* knockout mice and show that they have structural birth defects indicative of hedgehog signaling dysfunction. Surprisingly, ciliary assembly is not affected, but abnormal hedgehog signaling is observed in conjunction with ciliary accumulation of patched-1 and Smoothened. Similarly, Smoothened accumulates in cilia on cells mutated for BBSome components or the BBS binding protein/regulator Lztfl1. Interestingly, the BBSome and Lztfl1 accumulate to high levels in *Ift27* mutant cilia. Because *Lztfl1* mutant cells accumulate BBSome but not IFT27, it is likely that Lztfl1 functions downstream of IFT27 to couple the BBSome to the IFT particle for coordinated removal of patched-1 and Smoothened from cilia during hedgehog signaling.

INTRODUCTION

The cilium plays a key role in development by coordinating cell physiology with signals coming from the extracellular environment. Defects in ciliary structure or ciliary signaling underlie a diverse class of human diseases that range from adult onset degenerative disorders such as polycystic kidney disease, liver fibrosis, and retinal degeneration to structural birth defects of the heart, brain, and skeleton, to obesity and other metabolic disorders. The cilium functions by creating a cellular microenvironment where receptors and signaling pathways are sequestered and concentrated in a small projection from the surface of the cell. Cilia can detect many types of signals, from photons in rod and cone outer segments to diverse odorants detected by olfactory cilia, to mechanical stimuli detected by epithelial cilia or morphogenic ligands like sonic hedgehog (Shh) detected by the cilia of the developing embryo (Satir and Christensen, 2007).

Cilia themselves are extremely complex organelles that are composed of at least 500–1,000 structural proteins organized around a microtubule-based cytoskeleton and an associated membrane domain (Pazour et al., 2005). Many of the structural components of the cilium are known to be encoded by genes involved in human diseases, and the number of human disorders or syndromes caused by ciliary defects is rapidly growing (Badano et al., 2006). Understanding how this organelle is assembled and how the signaling environment is created and maintained is critical to understanding how the cilium functions in the etiology of these diseases. The cilium is assembled by the process of intraflagellar transport (IFT), where large protein complexes called IFT particles are carried along the ciliary microtubules by kinesin and dynein motors (Rosenbaum and Witman, 2002; Pedersen and Rosenbaum, 2008). The IFT particles are composed of more than 20 unique proteins organized in two subcomplexes called IFT-A and IFT-B (Cole et al., 1998; Ou et al., 2007; Follit et al., 2009). The IFT particles are thought to function as a cargo adaptor to connect proteins needed to build cilia to the molecular motors so the ciliary structural components can be transported from the cell body into the cilium for assembly. IFT-B appears to be critically important for ciliary assembly, as mutations in most IFT-B components block ciliary assembly. IFT-A mutations typically cause less severe defects in ciliary assembly and often result in accumulations of materials in the cilium, suggesting that it is more important for retrograde transport (Iomini et al., 2009). In addition to IFT-A and IFT-B, a third complex called the BBSome is connected to the IFT particle. Mutations in BBSome components do not typically block ciliary assembly but prevent the delivery of specific receptors to the cilium (Berbari et al., 2008) and cause accumulations of abnormal membrane-associated proteins in the cilium (Lechtreck et al., 2009).

In this work, we examine the function of the IFT-B subunit IFT27 (also known as Rabl4), which was recently shown to be mutated in two siblings with Bardet-Biedl syndrome (BBS). The

affected siblings displayed classic BBS phenotypes, including obesity, polydactyly, mental disabilities, renal dysfunction, and retinal degeneration (Aldahmesh et al., 2014). IFT27 is a small G protein distantly related to the Rab subfamily of Ras-like GTPases (Qin et al., 2007). The mammalian protein lacks the prenylation sites found in other Rab proteins, indicating that it is not membrane associated (at least via these moieties). Instead, IFT27 forms a stable heterodimer with IFT25 that exists both within the IFT-B complex and outside of it. IFT27 binds nucleotide with micromolar affinity but has a very low intrinsic GTPase activity (Bhogaraju et al., 2011). We became interested in IFT25 and IFT27 because, unlike most IFT-B proteins, these two subunits are missing from several species that assemble cilia. This suggested that IFT25 and IFT27 are not required for ciliary assembly but could be involved in sensory or other functions of cilia (Keady et al., 2012). We recently showed that IFT25 is not required for ciliary assembly, but mice homozygous for a null allele died at birth with a variety of structural defects (Keady et al., 2012). The *Ift25* phenotype differed from previously studied null alleles of IFT complex B proteins, as those alleles caused lethality earlier in development, typically at midgestation. In this study, we generated an *Ift27* mutant mouse model and showed that it has a phenotype overlapping that of the *Ift25* mutant. Using these two mutant mouse models, we show that *Ift25* and *Ift27* are dispensable for ciliogenesis, but both are required for BBSome trafficking essential for hedgehog signaling.

RESULTS

Ift27 Mutants Have Pleiotropic Structural Birth Defects

To understand the importance of IFT27 to ciliary assembly and mouse development, we used European Conditional Mouse Mutagenesis Program (EUCOMM) cells to create an *Ift27* mutant mouse (Figures 1, 2, 3, and 4). The $Ift27^{null1}$ allele (Figure S1 available online) that we analyzed for most studies (all except Figure 4H) contained a β-galactosidase gene in intron 2 and had exons 3–5 deleted. The β-galactosidase gene has a strong splice acceptor at its 5′ end and is expected to capture the upstream exons of *Ift27* to prevent their splicing to the downstream exons. It is likely that the $Ift27^{null1}$ allele is a null or a strong hypomorph, as quantitative RT-PCR indicated that transcripts containing the 3′ exons were reduced to less than 0.5% of controls (Figures 3A and 4A) and no protein was detected by western blot (Figures 3A and 4A). The expected Mendelian ratio of genotypes was found in animals harvested the day prior to birth (embryonic day [E]18) and on the day of birth (P0), but all homozygous mutants exhibited cyanosis and were stillborn or died shortly after birth (Figures 1A and 1B).

Fourteen *Ift27* mutant E18 embryos were analyzed by MRI (Table S1) and episcopic confocal microscopy (ECM) (Figure 2; Table S2), and 11 other E18 animals were analyzed by necropsy and histology (Figures 1 and 2; Table S3). The phenotypes observed in each animal are listed in Tables S1 through S3 and summarized here. Many of the same phenotypes observed in the *Ift25* mutants (Keady et al., 2012) were also observed in the *Ift27* mutant animals, but the phenotypes were more severe and more penetrant in the *Ift27* mutants. Like *Ift25*, *Ift27* mutants had a high incidence of omphaloceles or umbilical cord hernias. Polydactyly and other digit defects were observed in the *Ift27* mutants. In contrast to the *Ift25* mutant in which only preaxial duplication of digit 1 was observed, the *Ift27* animals also showed central polydactyly and syndactyly. *Ift27* mutants occasionally exhibited abnormal flexure of the wrists, resulting in a clubbing phenotype (talipomanus) (Figure 1J).

A small lower jaw (micrognathia) of varying severity was observed (Figures 1Cb and 1Cc), and most animals had an abnormally shaped nose (Figures 1C and 1E) with closely spaced eyes (hypotelorism) (Figure 1Cd). Morphological assessment of the cranial facial region showed hypoplasia of the midline, including nasal structures, maxilla, and mandible. Histological analysis indicated that the mutants lacked development of the palate, upper incisor, vomeronasal organ, and body of the mandible, with the development of a single anterior nasal aperture (Figure 1F). The latter anomaly appeared to develop as a result of a smaller, malformed nasal septum that failed to fuse with structures at the floor of the nose (Figure 1F). The *Ift27* mutants also developed various malformations of the tongue that ranged from aglossia (lack of tongue development) to microglossia (abnormally small tongue) to the tongue being abnormally attached to the floor of the oral cavity (Figure 1E; Table S1).

Like *Ift25*, *Ift27* mutants had malaligned sternal vertebrae and malformed ribs, yielding an abnormally shaped chest cavity (Figures 1G and 1H). Also similar to *Ift25* mutants, lung isomerisms (Figure 2A) and other structural respiratory tract abnormalities were prevalent in *Ift27* mutants. Fusions between the trachea and esophagus (tracheoesophageal fistulas; TEFs) were found in many *Ift27* mutants. The *Ift27* mutant lungs often contained a large abnormal balloon-like cavity (Figure 2Ad). ECM imaging revealed that these cavities arise from the bronchial airways after they branch from the fused tracheaesophagus, and the balloons then project through the diaphragm to connect with the stomach (Figure 2Ad). Histological analyses showed that multiciliated cells were present on the lining of the cavity (Figure 2B).

Cardiac malformations (Figures 2C, 2D, and S2) were found in all *Ift27* mutants. Similar to the *Ift25* animals, we observed a double-outlet right ventricle (Figure S2A; Movie S1), which was associated with hypoplasia of the pulmonary trunk (Figure S2B; Movie S2). The *Ift27* mutants, similar to the *Ift25* mutants, showed partial or complete atrioventricular septal defects (AVSDs) that reflect defects in development of the endocardial cushions. This resulted in a single orifice with common AV valves formed instead of separate tricuspid and mitral valves required for separation of the right atrium/right ventricle from the left atrium/left ventricle. In mutants with partial AVSD, the atrioventricular orifice is asymmetrically positioned to favor one ventricle (Figure 2D; Movie S1). These defects are also associated with a common atrium due to complete failure in atrial septum formation. In addition, one mutant exhibited a pulmonary artery defect where a long common artery extended from the pulmonary trunk (Figure S2D; Movie S2), and aortic arch anomalies were also observed with one mutant exhibiting a double arch forming a vascular ring (Figure S2F; Movie S3). The latter phenotype was observed in conjunction with TEFs. As with the *Ift25* mutants, *Ift27* mutant animals likely die neonatally from these severe congenital heart defects.

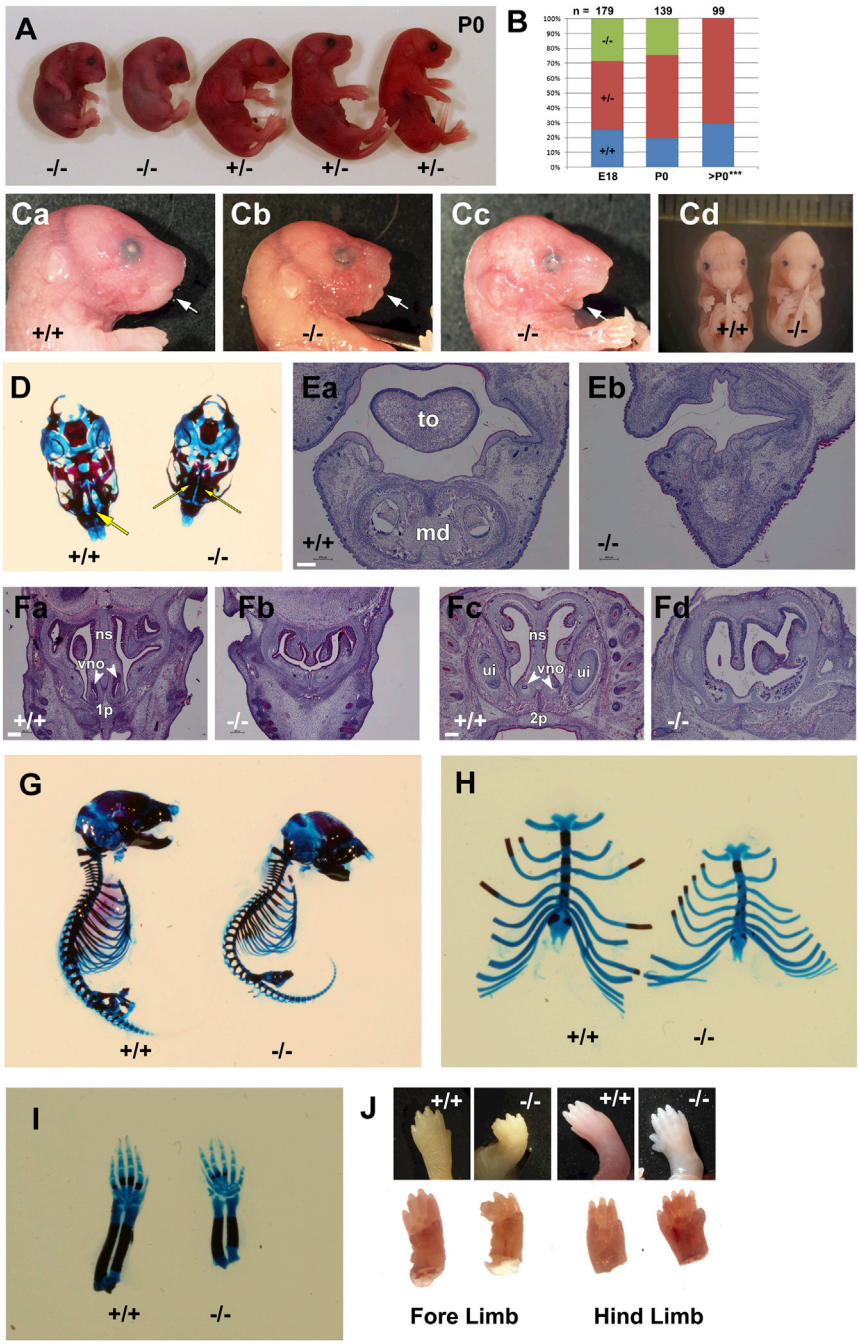

Figure 1. *Ift27* Null Mutants Display Multiple Developmental Defects

(A) Images of P0 animals. *Ift27*^{null1} genotypes are given below the images. All animals were alive when photographed.

(B) Genotype distribution at the day prior to birth (E18), day of birth (P0), and later (>P0) in offspring of *Ift27*$^{null1/+}$ × *Ift27*$^{null1/+}$ crosses. Blue, orange, and green represent +/+, +/−, and −/− genotypes, respectively. Homozygous mutant animals were alive on the day prior to birth but died on P0, so the P0 numbers reflect a mix of live and dead animals.

(C) Images of embryos at E18.5 (a–c) and E15.5 (d). Note abnormal facial structure, abnormal lower jaw (arrow), and more closely spaced eyes (hypotelorism).

(D) Alcian blue and alizarin red staining of the skull shows abnormal palate development.

(E) Hematoxylin-and-eosin (H&E)-stained frontal sections of the oral cavity. The mutant lacks the body of the mandible (md) and the tongue (to).

(F) H&E-stained sections of nasal cavities of E15.5 (a and b) and E18.5 (c and d) embryos. The mutant embryos in each case show underdeveloped nasal structures, particularly the inferior regions including the vomer bone of the nasal septum (ns), although superior cartilaginous parts of the septum appear to develop normally. 1p, primary palate; 2p, secondary palate; ui, upper incisor; vno, vomeronasal organ. Scale bars, 200 μm.

(G and H) Alcian blue and alizarin red staining of the skeleton shows abnormal skull shape, curvature of the spine and abnormal rib cage including malaligned sternal vertebrae.

(I and J) Alcian blue and alizarin red stained (I) and unstained (J) images of limbs showing a variety of digit defects.

Left lung isomerism was the only laterality phenotype observed in the *Ift25* mutants. This was observed in *Ift27* mutants, but the *Ift27* animals also show a variety of left-right patterning defects characterized by heterotaxy with randomization of visceral organ situs. Defects include malpositioning of the stomach (dextrogastria), liver isomerisms, and cardiac malformations. Laterality defects of the heart include abnormal positioning of the organ (dextrocardia and mesocardia) (Figure 2C), right atrial isomerism, and duplication of the inferior vena cava (Figure S2F; Movie S4).

IFT27 Is Not Required for IFT25 Stability but Is Required for IFT25 Entry into Cilia

IFT25 was not required for ciliary assembly or for the stability of any of the IFT particle proteins that we have antibodies against, except for IFT27, which is largely depleted when IFT25 was lost (Keady et al., 2012). Similarly IFT27 is not required for ciliary assembly in cultured fibroblasts or in the embryo (Figure 3). As expected, IFT27 protein is missing from the *Ift27* mutant cells, as detected by western blot and by immunofluorescence (IF) staining. The abundance of IFT25 is not affected by the loss of IFT27 (Figure 3A), indicating that, while IFT27 requires IFT25 for stability, the requirement is not mutual. The levels of some complex B proteins (IFT88, IFT57) were reduced in the *Ift27* mutant cells, but the significance of this is not clear, as ciliation is normal and IFT88 staining of mutant cilia is similar to that of wild-type (Figures 3B–3D). In *Trypanosoma*, *Ift27* RNA interference caused a reduction of IFT dynein and IFT-A proteins and an increase in IFT-B proteins in the cilia (Huet et al., 2014). However, we did not observe any differences in IFT dynein (Dync2h1),

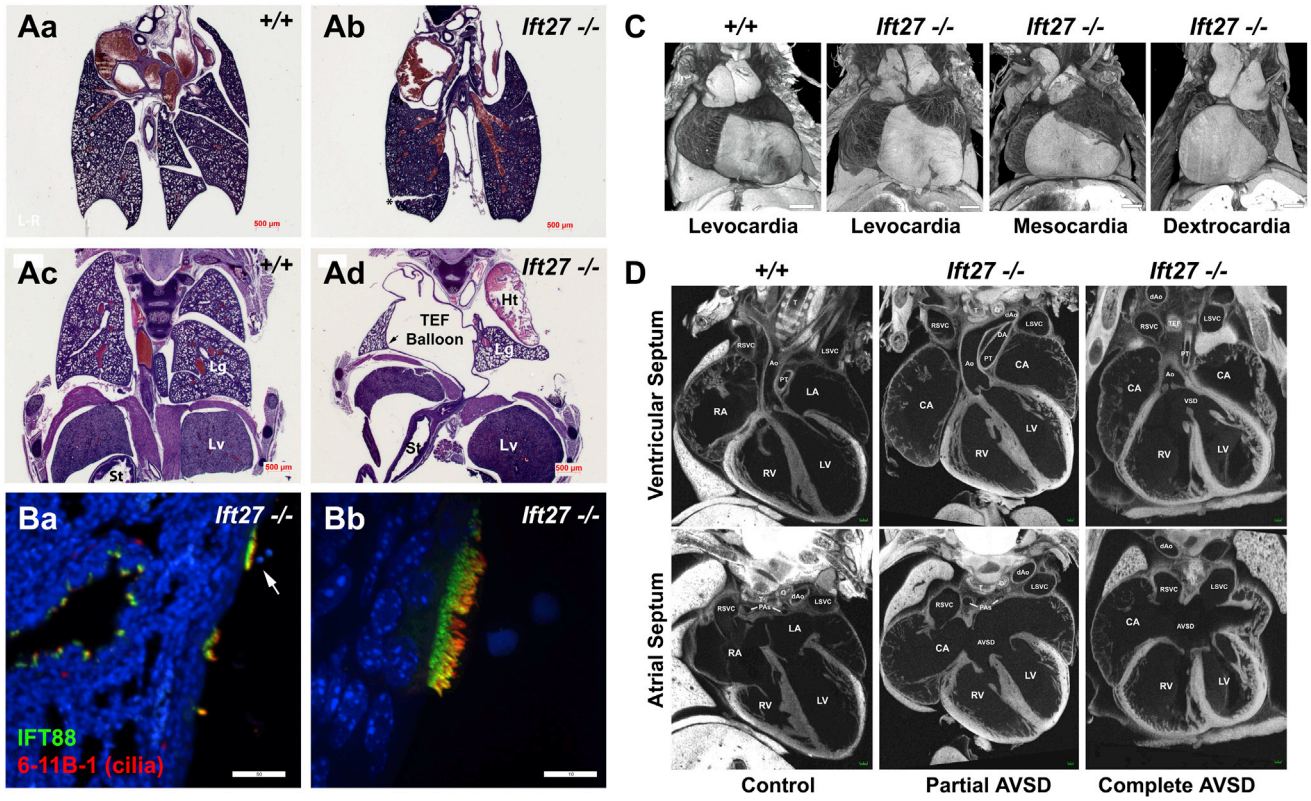

Figure 2. *Ift27* Mutants Have Structural Heart and Lung Diseases

(A) Lung isomerism. H&E images show the normal arrangement of four right lobes and one left lobe in the control animals (a and c). Mutants (b and d) have a single lobe on both sides, indicating a left isomerism. Note the large open sac (TEF balloon) within the thoracic cavity that projects through the diaphragm and connects to the stomach (St). Lg, lung; Lv, liver; Ht, heart. Scale bars, 500 μm. The asterisk indicates a crack in the tissue that occurred during processing.

(B) IF images of the epithelium lining the TEF balloon (IFT88, green; 6-11B-1, red; DAPI, blue). A section adjacent to the one imaged in (d) was stained, and the approximate position of the imaged region is indicated by an arrow in (d). Likewise, the arrow in (a) indicates the cell that was imaged in (b). Scale bars, 50 μm in (a) and 10 μm in (b). (a) and (b) are maximum projections of a 16- and 10-layer z stacks acquired every 0.5 μm.

(C) Surface renderings of ECM image stacks show heart placement defects. The apex of the heart normally points toward the left side of the thoracic cavity (levocardia). Heart orientation in *Ift27* mutants is variable with 11/14 showing levocardia, 1/14 showing mesocardia (apex at midline), and 2/14 showing dextrocardia (apex pointed to the right side).

(D) ECM imaging reveals structural heart defects in *Ift27* mutants. Images shown are single planes of reconstructed hearts taken at levels to highlight the ventricular septum (top row) or atrial septum (bottom row). Movies of these 3D reconstructions and additional planes are included in the Supplemental Information. The left panels show control heart images, and the middle and right panels are from mutants illustrating either partial (middle) or complete (right) atrioventricular septal defects. CA, common atrium; VSD, ventricular septal defect; Ao, aorta; dAo, descending aorta; PT, pulmonary trunk; PA, pulmonary artery; LSVC, left superior vena cava; RSVC, right superior vena cava; LA, left atrium; RA, right atrium; LV, left ventricle; RV, right ventricle; T, trachea; O, esophagus.

IFT-A (IFT140), or IFT-B (IFT88) distribution in our cells (Figure 3C). We were unable to determine if the endogenous distribution of IFT25 was altered in *Ift27* cells, as neither a commercial antibody nor any that we generated worked for IF (Figure S3). However, Flag-IFT25 was unable to enter cilia on *Ift27* mutant cells but was able to enter wild-type cells (Figure 3E), suggesting that, while IFT25 is stable in the absence of IFT27, it does not bind the IFT particle. Direct interaction between IFT25 and IFT27 appears to be important for the delivery of IFT25 to cilia, as mutation of three residues (T40R/T42R/S128E) in IFT25 that make direct contact with IFT27 (Bhogaraju et al., 2011) disrupts the interaction as detected by immunoprecipitation and prevents the entry of IFT25 into cilia (Figures 3F and 3G). This mutation also fails to rescue the Smo1 and BBS9 accumulation defects (discussed later) caused by the loss of IFT25 (Figure 3H).

IFT27 is a small G protein in the RAS superfamily and, as such, is thought to bind and hydrolyze guanosine triphosphate (GTP) (Qin et al., 2007; Bhogaraju et al., 2011). To understand how the GTP/guanosine diphosphate (GDP) state of IFT27 affects binding of IFT27 to IFT25 and the IFT particle, we generated IFT27 constructs with the mutations that are expected to mimic the GTP-bound (K68L) and GDP-bound or nucleotide-free (T19N) states. These mutations in IFT27 did not affect binding to IFT25 (Figure 3I), indicating that the GTP cycle does not influence the formation of the IFT25/IFT27 heterodimer. The binding of IFT27 to the IFT particle (IFT88) was disrupted by the $Ift27^{T19N}$ mutation but not by the $Ift27^{K68L}$ mutation (Figure 3I). Consistent with this, in wild-type cells, $IFT27^{T19N}$ was excluded from cilia (Figure 3J, top row). However, $IFT27^{T19N}$ was able to enter the cilia of *Ift27* mutant cells (Figure 3J, bottom row), suggesting that it retains some ability to bind the IFT particle but that the

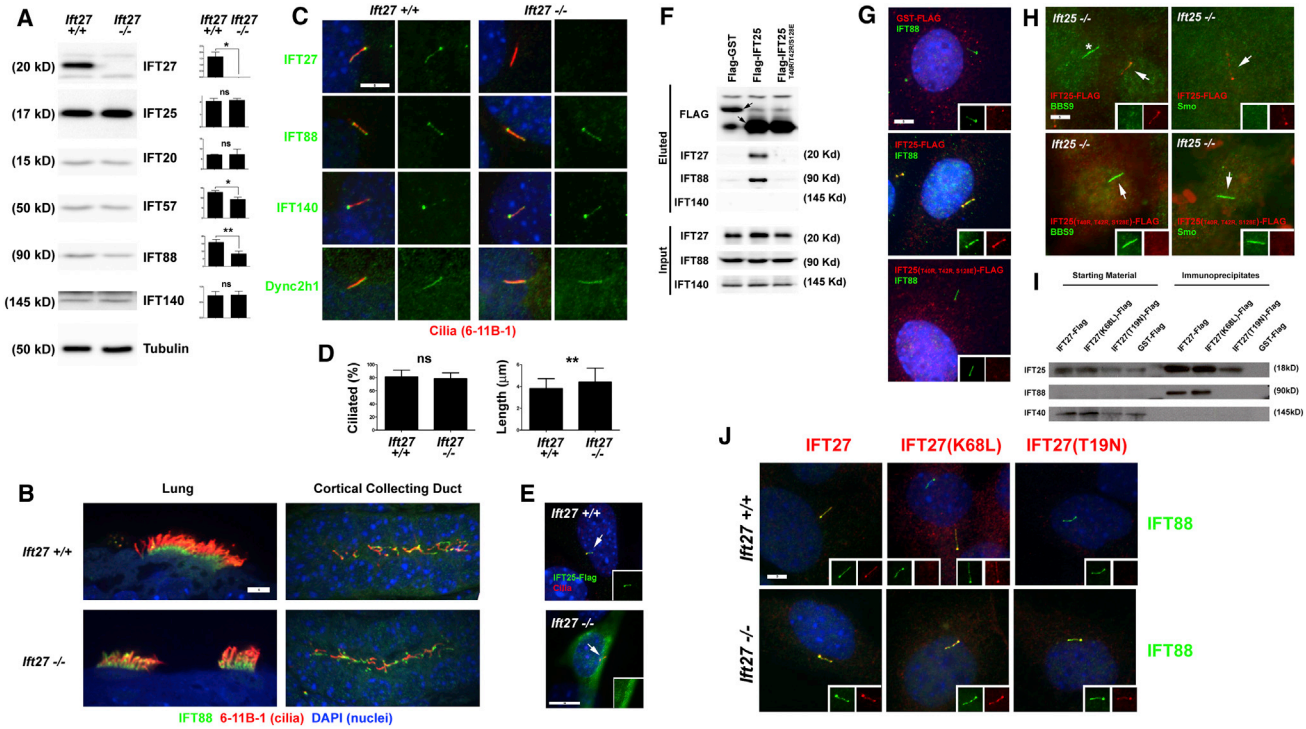

Figure 3. *Ift27* Is Not Required for Ciliation

(A) Effect of the *Ift27*^{null1} mutation on IFT protein stability. Protein extracts from wild-type and mutant MEFs were immunoblotted with the antibodies indicated on the right side of each western blot panel. Approximate molecular weights are listed on the left side. Quantitation of IFT protein levels relative to γ-tubulin loading control are listed on the right side of each western blot (n = 3 embryos/MEF lines per genotype) (*p < 0.05; **p < 0.01). Error bars indicate SD.

(B) E18.5 lung and kidney sections from *Ift27*$^{+/+}$ and *Ift27*$^{null1/null1}$ mice immunostained with IFT88 (green) and the acetylated tubulin cilia marker 6-11B-1 (red). Scale bar, 5 μm and applies to all images. Images are maximum projections of ten-layer z stacks acquired every 0.5 μm.

(C) IF of control and mutant MEFs immunostained with 6-11B-1 (cilia, red) and IFT27, IFT88, IFT140, or Dync2h1 (green). Note the lack of IFT27 staining of mutant cells (25/25 wild-type cells and 0/25 mutant cells showed IFT27 staining). Staining of cilia for the other antibodies were similar in both mutant and control cells (25/25 cells positive for each condition).

(D) Quantitation of ciliation and ciliary length in MEF cells. Percentage of ciliated cells and ciliary lengths based on ciliary IFT88 immunostaining in serum-starved MEFs (n = 3 *Ift27*$^{+/+}$ and 3 *Ift27*$^{null1/null1}$ embryos/MEF lines for percent ciliation and n = 50 cilia per cell line for length). Differences for percent ciliation were not significantly different, but mutant cilia were slightly longer (**p < 0.01; ns, not significant). Error bars indicate SD.

(E) IFT25-Flag (green) localizes to cilia (6-11B-1, red) in wild-type cells but not *Ift27*$^{null1/null1}$ cells. Inset shows green (IFT25-Flag) channel. Quantification shows that 23/25 transfected wild-type cells had ciliary-localized IFT25-Flag while 0/25 transfected mutant cells had ciliary-localized IFT25-Flag.

(F and G) Interaction between IFT25 and IFT27 are required for IFT25 to enter cilia. (F) Immunoprecipitation from IMCD3 cells transfected with Flag-GST, Flag-IFT25, or Flag-IFT25(T40R/T42R/S128E) demonstrates that wild-type IFT25, but not the mutant form, binds to IFT27 and IFT88. (G) In IMCD3 cells, wild-type Flag-IFT25 (Flag, red) localizes to cilia (IFT88, green), but Flag-IFT25(T40R/T42R/S128E) (Flag, red) does not. Quantification shows that 0/50 Flag-GST-, 47/50 Flag-IFT25-, and 0/50 Flag-IFT25(T40R/T42R/S128E)-transfected cells had Flag-positive cilia. Scale bar, 5 μm and applies to all images in (G).

(H) Wild-type Flag-IFT25 (top row; Flag, red), but not Flag-IFT25(T40R/T42R/S128E) (bottom row; Flag, red), rescues the BBS9 (left panel, green) and Smo (right panel green) accumulation phenotypes in *Ift25*$^{null1/null1}$ mutant MEFs. Arrows indicate cilia on transfected cells, which are shown in the insets with separate red and green channels. Quantification of 25/25 cells transfected with wild-type IFT25 showed rescue of the accumulation of ciliary BBS9 and Smo phenotypes, while 0/25 transfected with IFT25(T40R/T42R/S128E) showed rescue. Asterisk indicates a cilium on a nontransfected cell. Scale bar, 5 μm and applies to all images.

(I) Immunoprecipitation from MEF cells transfected with IFT27-Flag, IFT27(K68L)-Flag, IFT27(T19N)-Flag, or Flag-GST demonstrates that all forms of IFT27 bind to IFT25 but only wild-type and the K68L forms of IFT27 bind to IFT88. No binding between any form of IFT27 and IFT140 was detected. Note that, with this exposure time, IFT88 is not detectable until after immunoprecipitation.

(J) Wild-type IFT27-Flag (left column; Flag, red), IFT27(K68L)-Flag (middle column; Flag, red) and Flag-IFT27(T19N) (right column; Flag, red) expressed in *Ift27*$^{+/+}$ (top row) and *Ift27*$^{null1/null1}$ (bottom row) MEFs. Quantification showed that 80/100 IFT27-Flag-, 24/100 IFT27(K68L)-Flag-, and 0/100 IFT27(T19N)-Flag-transfected *Ift27*$^{+/+}$ cells had Flag-positive cilia, while 72/100 IFT27-Flag-, 86/100 IFT27(K68L)-Flag-, and 36/100 IFT27(T19N)-Flag-transfected *Ift27*$^{null1/null1}$ cells had Flag-positive cilia. Scale bar, 5 μm and applies to all images.

affinity is reduced such that it cannot compete with wild-type. Furthermore, *Ift27*^{T19N} was not able to fully rescue the Smo1 and BBS9 accumulation defects (discussed later) caused by the loss of IFT27, while wild-type *Ift27* and *Ift27*^{K68L} were able to rescue (Figure S3C). Thus, it is likely that IFT27 is in the GTP-bound state in the cilium, and the data further suggest that the IFT particle is an effector of IFT27, since the interaction is affected by the GTP/GDP state of IFT27.

Ift27 Mutants Have Hedgehog Signaling Defects

It is well established that cilia play a major role in the hedgehog pathway of the developing embryo (Huangfu et al., 2003), and

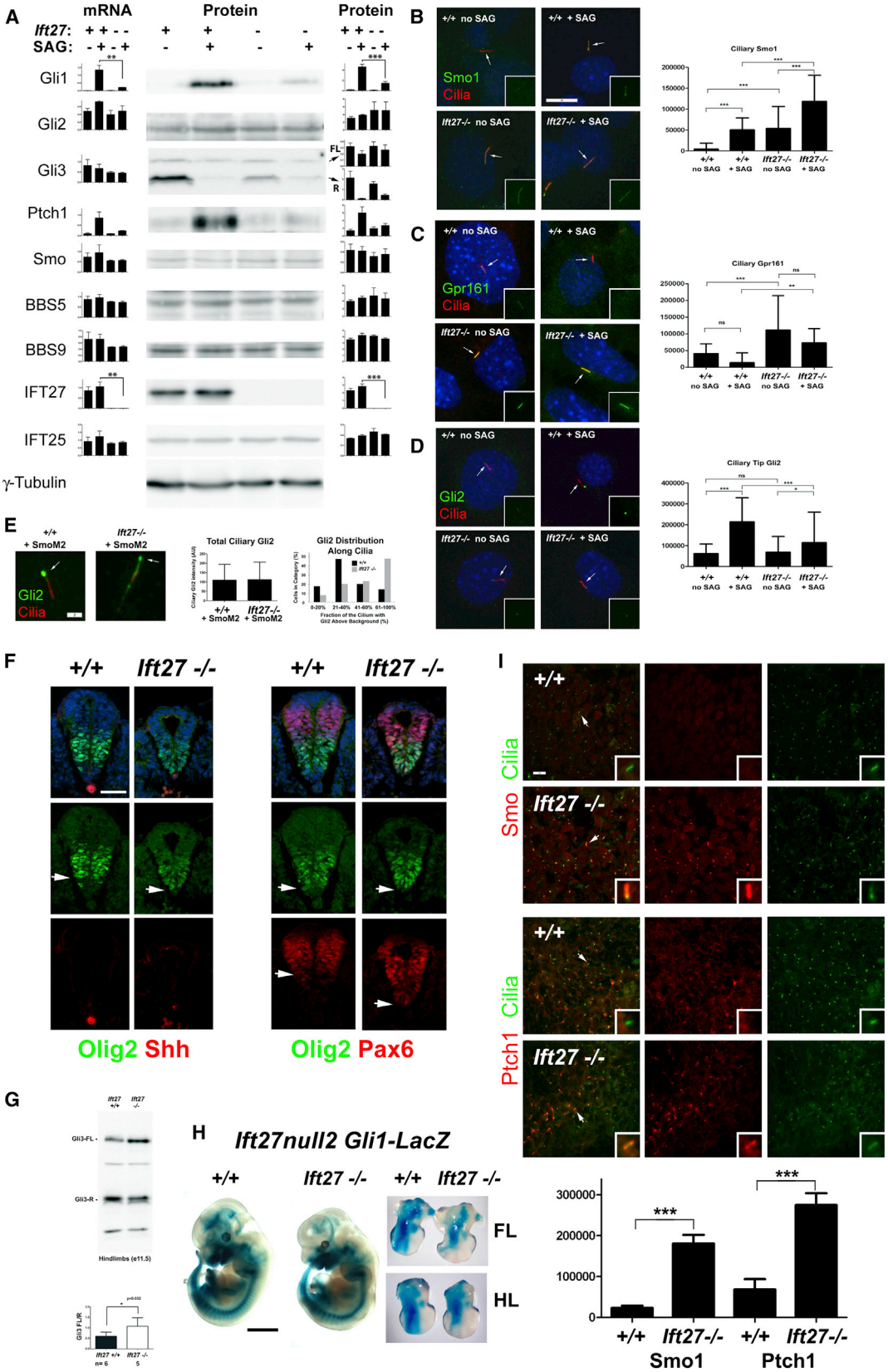

(legend on next page)

many of the phenotypes observed in the *Ift27* mutant mouse are consistent with defects in hedgehog signaling. Thus, we analyzed how hedgehog signaling was affected by the loss of IFT27 in the developing embryo and in vitro cultured fibroblasts. Analysis of cultured murine embryonic fibroblasts (MEFs) (Figure 4A) showed that, while *Gli1* is highly upregulated in response to the hedgehog activator Smoothened Agonist (SAG) in wild-type cells, the response is dampened significantly in the mutant cells. *Ptch1* behaved similarly, but the high amount of variation in expression precluded reaching statistical significance. This attenuation was similar to what we observed in *Ift25* and *Ift88* mutant cells (Keady et al., 2012). The response was observed at both the messenger RNA and protein levels. As expected, other genes (Gli2, Smo, etc.) not transcriptionally activated by the hedgehog pathway were not affected.

When the hedgehog pathway is normally activated, Ptch1 and Gpr161 exit from the cilium and Smo and Gli2 enter. *Ift27* mutants are defective in maintaining low ciliary Smo levels when the pathway is off (Figure 4B). Interestingly, additional Smo can enter the cilium when the pathway is activated by SAG. This additional accumulation is likely because SAG activates the pathway by binding Smo directly (Chen et al., 2002) and does not depend on activation of the upstream parts of the pathway. Similar to what we observed in cultured cells, Smo accumulates to high levels in the cilia of the embryo, which is also the case for Ptch1 (Figure 4I). Gpr161 is normally found in unstimulated cilia and exits after pathway activation (Mukhopadhyay et al., 2013). In *Ift27* mutants, more Gpr161 is present in the cilia than normal at the basal state, and the protein is not fully cleared after activation (Figure 4C). Even though SAG is capable of stimulating the entry of additional Smo and partial removal of Gpr161 in *Ift27* mutant cells, this is not sufficient to cause Gli2 to accumulate at the ciliary tip in normal levels (Figure 4D). The failure of Gli2 to accumulate at the ciliary tip could be caused by the lack of signal from the upstream components of the pathway or because IFT27 is needed to transport Gli2 into the cilium. To distinguish between these possibilities, we transfected wild-type and *Ift27* mutant cells with SmoM2. SmoM2 is an oncogenic form of Smo that is constitutively activated (Xie et al., 1998). Expression of SmoM2 in wild-type cells caused Gli2 accumulation at the ciliary tip, similar to what would be observed if the pathway were activated (Figure 4E). *Ift27* mutant cells transfected with SmoM2 accumulated ciliary Gli2 to the same level as that of the control cells. However, in the mutant cells, the Gli2 was more broadly distributed along the length of the cilium rather than being concentrated at the tip. This suggests that IFT27 is not needed for entry of Gli2 into the cilium but is needed for its transport to the tip or alternatively in some yet-unknown structural aspect of the ciliary tip.

In vivo analysis of the hedgehog pathway in mouse neural tube showed caudal expansions of Olig2- and Pax6-positive cells and a failure of the floor plate to express sonic hedgehog (Figure 4F). These phenotypes are similar to what we saw in the *Ift25* mouse, similar to other IFT complex B mutant mice (Keady et al., 2012; Ko et al., 2009), and are consistent with the attenuated hedgehog signaling observed in vitro. The processing of Gli3 into the repressor form was also reduced in the *Ift27* mutants (Figure 4G) similarly to how it is affected by *Ift25* and other IFT complex B mutants (Keady et al., 2012; Haycraft et al., 2005). To understand how the *Ift27* mutation affects global hedgehog signaling, Gli1-LacZ expression was monitored in E12.5 embryos. Note that the *Ift27* allele ($Ift27^{null2}$) used in this experiment did not contain a β-galactosidase gene (Figure S1). Alterations in Gli1-LacZ expression were observed in the brain, limb buds, and facial regions, consistent with these regions being the most highly affected by the lack of IFT27 (Figure 4H and Figure S4).

Ift27 Mutants Accumulate BBS Proteins in Cilia

Much the same as what we observe in *Ift25* and *Ift27* mutant cells, Ptch1 and Smo accumulate in the cilia of *Bbs* mutant cells (Zhang et al., 2012) (Figure S5), prompting us to examine how the BBSome is affected by the *Ift27* mutation. In wild-type cells, the

Figure 4. IFT27 Is Required for Normal Hedgehog Signaling

(A–D) In (A)–(C), $Ift27^{+/+}$and $Ift27^{null1/null1}$ MEFs were left untreated or treated with SAG, a Shh pathway activator. Cell lines from three different embryos were used for each genotype. (A) RNA was isolated from one set of cells and analyzed for gene expression by quantitative real-time PCR (left column). Proteins were isolated from another set of cells and analyzed by western blotting. Quantitation of protein levels are listed on the right side of each western blot and compared to γ-tubulin loading control. Groups were compared by ANOVA; only comparisons between SAG-treated control and mutant cells are depicted in this figure (**$p \leq 0.01$; ***$p \leq 0.001$), but other comparisons are shown in Table S4. Full-length (FL) and repressor (R) forms of Gli3 protein were analyzed separately. In (B)–(D), cells were fixed and stained for cilia (arrows; 6-11B-1, red) and Smo (green, B), Gpr161 (green, C), or Gli2 (green, D). Insets show the green channel (Smo, Gpr161, or Gli2). Ciliary Smo or ciliary tip Gli2 was quantitated in 25 cilia from three independent cell lines of each genotype. Ciliary Gpr161 was quantitated in 25 cilia from one cell line of each genotype. Groups were compared by ANOVA (*$p \leq 0.05$; **$p \leq 0.01$; ***$p \leq 0.001$; ns, not significant). Cilia length and percent ciliation for these cells are shown in Figure 3D. Scale bars, 10 μm and apply to all images in (B)–(D). Error bars in (A) indicate SEM; all other error bars indicate SD.

(E) $Ift27^{+/+}$and $Ift27^{null1/null1}$ MEFs were transfected with SmoM2-mCherry and fixed and stained for cilia (6-11B-1, red) and Gli2 (green). Note the concentration of Gli2 at the ciliary tip (arrow) of control cells as compared to the broader distribution in the mutant cell. Total Gli2 was quantitated from >100 cilia and was not significantly different in the two groups. The distribution of Gli2 along the cilium was quantitated by determining what percentage of the cilium length had Gli2 fluorescence intensity above background. Scale bars, 2 μm and apply to all images.

(F) Neural tube patterning of $Ift27^{null1/null1}$ embryos. All images are shown with the ventral side (floor plate) on bottom. Cryosections were cut from caudal regions of E9.5 embryos and immunostained for Olig2 (green) and Shh or Pax6 (red). Merged images with DAPI (blue) are shown in the top row. Arrows depict the absence of Pax6 and Olig2 in the wild-type floor plate and an expansion of Pax6 and Olig2 into the mutant floor plate. Scale bar, 50 μm and applies to all images.

(G) $Ift27^{+/+}$and $Ift27^{null1/null1}$ protein extracts from E11.5 hindlimbs were immunoblotted for Gli3 protein (Gli3-FL: full-length and Gli3-R: repressor). Quantitation of Gli3 protein levels (ratio of Gli3-FL/Gli3-R) from hindlimbs is shown below the gel (*p = 0.032). Number of embryos (n) analyzed is given below genotypes.

(H) E12.5 $Ift27^{null2}$, Gli1-LacZ embryos were fixed and stained for β-galactosidase activity. $Ift27^{null2}$ genotypes are provided above the embryos. Isolated limb buds are shown on the right side. Additional images are in Figure S4. Scale bar, 2 mm and applies to whole embryos. FL, forelimb, HL, hindlimb.

(I) Paraxial mesoderm stained with Smo and Ptch1 antibodies. Sections of E10.5 embryos were stained for cilia (6-11B-1, green) and either Smo or Ptch1 (red). Insets are 4× enlargements of the cilium indicated with an arrow. Scale bar, 10 μm. Images are maximum projections of 16-layer z stacks acquired every 0.25 μm. Graph at bottom shows ciliary Smo and Ptch1 are significantly (***$p < 0.001$) increased in the mutant embryos.

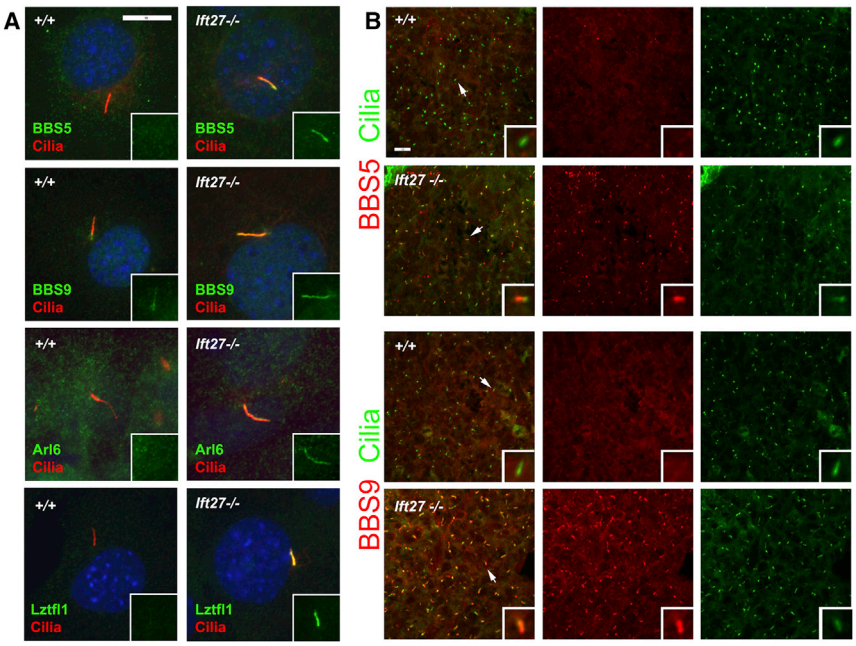

Figure 5. BBSome Subunits BBS5 and BBS9 and BBS Regulators Arl6 and Lztfl1 Accumulate in *Ift27* Mutant Cilia

(A) *Ift27*$^{+/+}$and *Ift27*$^{null1/null1}$ MEFs were stained for cilia (6-11B-1, red) and BBS5 (top row, green), BBS9 (second row, green), Arl6 (third row, green), or Lztfl1 (bottom row, green). Insets show the green channel (BBS5, BBS9, Arl6, Lztfl1). Quantification showed that 0% wild-type cells had detectable BBS5 in cilia, while 88% ± 12% of mutant cells had detectable BBS5 in cilia, and 0% wild-type cells had strong BBS9 in cilia (all had weak ciliary staining, with moderate staining of the centrosomal region), while 95% ± 6% of mutant cells had strong staining of BBS9 in cilia and no staining of the centrosome ($n = 25$ cilia from three cell lines per genotype, $p < 0.001$). Similarly 0% of wild-type cells had detectable Arl6 in cilia, while 80% ± 3% of mutant cells had detectable Arl6 in cilia, and 0% of wild-type cells had detectable Lztfl1 in cilia, while 97% ± 2% of *Ift27* mutant cells had strong Lztfl11 label in cilia ($n > 25$ cilia per genotype from three experiments, $p < 0.001$). Scale bar, 10 μm and applies to all images.

(B) Paraxial mesoderm stained with BBS5 and BBS9 antibodies. Sections of E10.5 embryos were stained for cilia (6-11B-1, green) and either BBS5 or BBS9 (red). Insets are 4× enlargements of the cilium indicated with an arrow. Scale bar, 10 μm. Images are maximum projections of 16-layer z stacks acquired every 0.25 μm.

BBSome subunit BBS5 is not detectable in cilia with our antibody, and the BBSome subunit BBS9 is found primarily at the base of the cilium with very faint label along the ciliary shaft. Interestingly, in *Ift27* mutant cells, both of these proteins accumulate to high levels in the cilium, so that BBS5 is easily detected and BBS9 is redistributed from the base of the cilium into the cilium (Figure 5A). This accumulation also is observed in *Ift*25 mutant cells (data not shown). Similarly BBS5 and BBS9 are not detectable on cilia in the paraxial mesoderm of wild-type embryos but are highly enriched in these cilia on *Ift27* mutant embryos (Figure 5B). These data suggest that the BBSome enters cilia independent of IFT25/IFT27 but requires them for removal.

Ciliary levels of the BBSome are regulated by Lztfl1 and the small GTPase Arl6, which is also known as BBS3. Lztfl1 is a BBSome-binding protein that was found in the cell body but not in the cilium. Knockdown cells accumulate high levels of the BBSome in their cilia, suggesting that Lztfl1 functions in the cell body to negatively regulate entry of the BBSome into cilia (Seo et al., 2011). Arl6 is required for entry of the BBSome into cilia and knockdown cells have reduced levels of ciliary BBSome (Jin et al., 2010). Interestingly, both Arl6 and Lztfl1 are highly enriched in *Ift27* mutant cilia (Figure 5A), suggesting that both proteins cycle through the cilia and that IFT25/IFT27 are needed for their removal. Like *Ift25* and *Ift27*, *Lztfl1* is conserved in *Chlamydomonas* but absent from *Drosophila* and *Caenorhabditis*. The *Chlamydomonas* homolog of Lztfl1 (XP_001696645.1) was found in our flagellar proteome (CrFP C_1570028, three peptides). The Ltzfl1 peptides were found in the membrane and matrix fraction, which is where IFT proteins fractionate (Pazour et al., 2005), suggesting that, in contrast to conclusions of prior studies (Seo et al., 2011), Lztfl1 is a ciliary protein. *Lztlfl1* mutant mice are not available, so we created *Ltzfl1* null NIH 3T3 lines using the clustered regularly interspaced short palindromic repeat (CRISPR)/Cas9 system (Cong et al., 2013). In these cells, Ltzfl1 protein was not detectable by western blotting (Figure 6A), and the cells showed Smo and BBSome accumulation as previously reported in knockdown cells (Seo et al., 2011) (Figure 6C). Ciliary assembly appeared normal, and the *Lztfl1* mutant cells had normal IFT27 ciliary staining (Figures 6B and 6C), suggesting that Lztfl1 functions downstream of IFT27. Previously, it was shown that a C-terminal fragment of Lztfl1 bound the BBSome and acted as a dominant-negative mutation, causing accumulation of BBSome components into cilia (Seo et al., 2011). Interestingly, the C-terminal half of Lztfl, which functions as a dominant-negative mutation, is trafficked to cilia, whereas the N-terminal half, which does not function as a dominant-negative mutation (Figure 6D), is not found in cilia. Neither fragment affected the distribution of IFT27 (data not shown), supporting a role of Lztfl1 downstream of IFT27.

To further understand the relationship between IFT27 and the BBSome in regulating the ciliary distribution of hedgehog components and the BBSome, we examined MEF cell lines mutated for BBSome components BBS2 and BBS7 and the BBS regulator BBS3/Arl6 (Figure S5). As expected, in all lines, the BBS components were not enriched in cilia, and all lines had increased levels of ciliary Smo. None of these cells lines had detectable alterations in IFT27 or Lztfl1 distribution, suggesting that IFT27 and Lztfl1 function upstream of the BBSome. The observations that mutations in *Bbs2*, *Bbs7*, *Lztfl1*, and *Ift27* all cause increases in ciliary Smo—while mutations in *Lztfl1* and *Ift27* cause increases in ciliary BBSome and mutations in *Ift27* alone causes increased ciliary Lztfl1 (Figure 7A)—suggest a

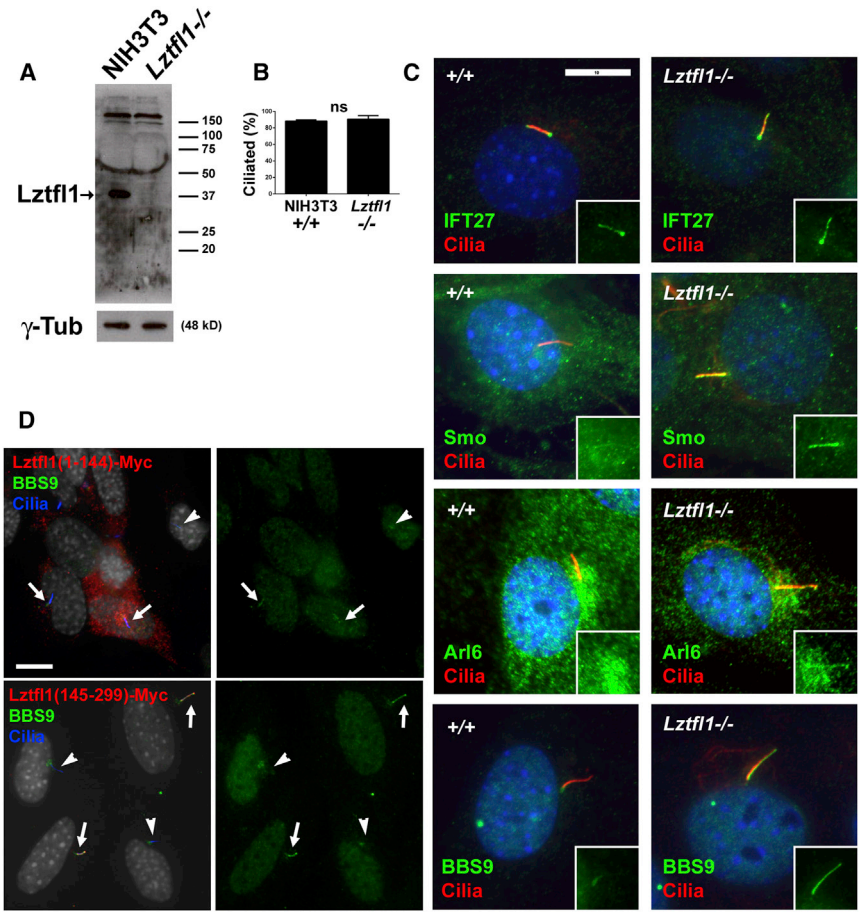

Figure 6. The BBSome Regulator Lztfl1 Functions Downstream of IFT27 in the Removal of the BBSome and Smo from Cilia

(A) NIH 3T3 control (+/+) and *Lztfl1* mutant (−/−) cells probed for Lztfl1 show that the mutant does not have any detectable protein. γ-tubulin is a loading control. Note that the blot is overexposed to ensure that no protein remains.

(B) Ciliation is not affected by the loss of Lztfl1 (n = 3 experiments on one cell line). Error bars indicate SD.

(C) NIH 3T3 control (+/+) and *Lztfl1* mutant cells were stained for cilia (6-11B-1, red) and IFT27 (top row, green), Smo (second row, green), Arl6 (third row, green), or BBS9 (bottom row, green). Insets show the green channel (IFT27, Smo, Arl6, BBS9). Scale bar, 10 μm. Quantification showed that 100% of control cilia and *Lztfl1* mutant cilia had normal IFT27 label (strong peribasal body label with weaker ciliary shaft label) (n = 3 experiments on one cell line per genotype); 4.0% ± 4% of control and 60% ± 11% of *Lztfl1* mutant cells had ciliary Smo label in unstimulated cells (n = 3 experiments on one cell line per genotype, $p < 0.01$); 0% of control cilia and 59% ± 26% of *Lztfl1* mutant cilia had weak but detectable levels of Arl6 (n = 3 experiments on one cell line per genotype, $p < 0.05$); and 0% of control cilia and 98% ± 2% of *Lztfl1* mutant cilia had strong ciliary BBS9 label (n = 3 experiments on one cell line per genotype, $p < 0.001$).

(D) The N-terminal half of Lztfl1 (residues 1–144) does not localize to cilia and does not perturb ciliation or increase the ciliary levels of BBS9. Quantification showed that 0/10 ciliated transfected cells had detectable ciliary BBS9. The C-terminal half of Lztfl1 (residues 145–299) localizes to cilia and causes BBS9 to accumulate in cilia. Quantification showed that 10/10 ciliated transfected cells had detectable ciliary BBS9. Arrows indicate cilia on myc-positive cells, and arrowheads indicate cilia on myc-negative cells. Scale bar, 10 μm.

model where Lztfl1 couples the BBSome to IFT25/IFT27 for removal from the cilium by retrograde transport (Figure 7B).

DISCUSSION

Why does the IFT particle need 6 complex A, 16 complex B, and 8 BBSome proteins to carry out its work? The high degree of evolutionary conservation from algae to humans suggests that each has an important function to play in the assembly of the cilium or in the signaling functions of the organelle. Trying to understand the functions of individual subunits has been a challenge, as mutations in most subunits disrupt the function of their respective subcomplexes. For example, in mouse, null mutations in most complex B subunits block ciliary assembly and result in embryonic lethality at midgestation. In contrast, the IFT25/IFT27 dimer appears to be a submodule of complex B, and its loss does not disrupt cilia assembly. In trypanosomes, IFT27 is required for IFT as cells depleted of the protein accumulate complex B proteins in short, stumpy flagella (Huet et al., 2014). The difference between IFT27 function in trypanosomes and mouse is unknown, but the fact that *Ift27* mutations do not block ciliary assembly in the mouse allowed us to uncouple the function of IFT25/IFT27 from the function of complex B in ciliary assembly. *Ift25* and *Ift27* mutant mice survive to birth but die soon after with a constellation of phenotypes including heart, lung, skeletal, and brain abnormalities. The phenotypes of the *Ift27* and *Ift25* mutants are similar, but the *Ift27* phenotypes are stronger and more penetrant. This was unexpected, as IFT27 is highly destabilized in the *Ift25* mutant and the protein was mostly gone. However, a small amount of IFT27 remains in the *Ift25* mutant animals, whereas no IFT27 is detected in the $Ift27^{null1}$ mutant, and it is likely that the small amount of IFT27 that remains in the *Ift25* mutant animals is able to partially function. The mouse *Ift27* phenotype suggests weakened hedgehog signaling, and we observed dysfunctional hedgehog signaling in both the embryo and in fibroblasts derived from the animals.

Model for the Function of IFT25/IFT27

Our finding that the IFT25/IFT27 dimer is not required for ciliary assembly but is needed to remove Smo when hedgehog signaling is off and to remove Ptch1 and Gpr161 when the pathway is activated raises the question about how IFT25 and IFT27 function to accomplish this.

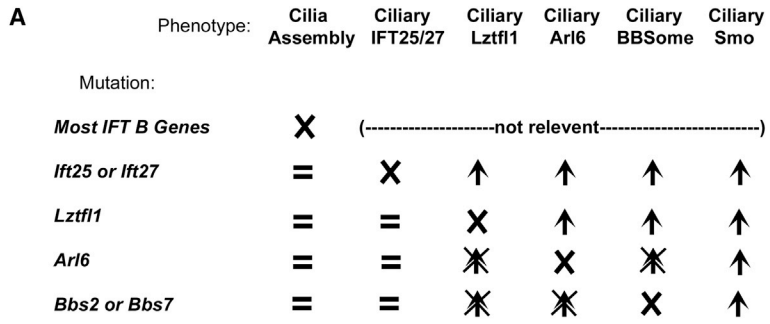

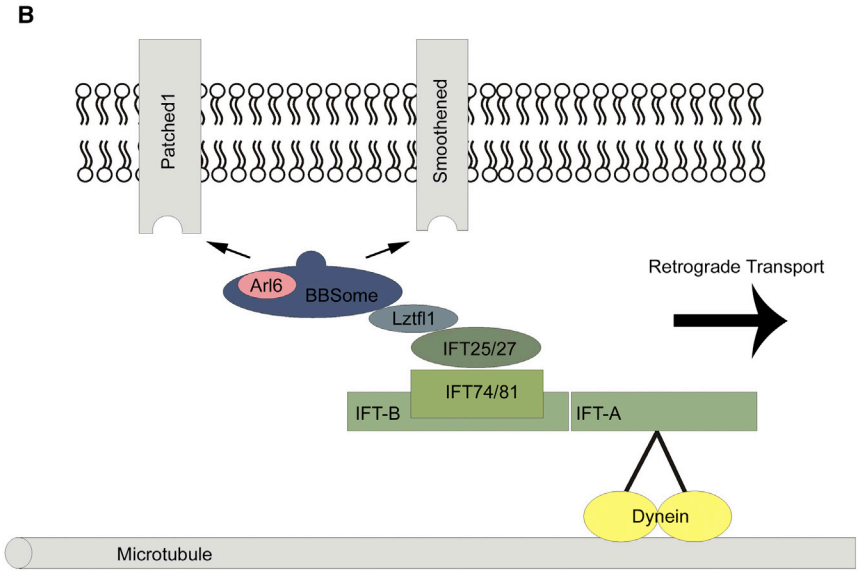

Figure 7. Model for IFT25/IFT27 Function

(A) Graphical summary of the effects of *Ift* and *Bbs* mutations on ciliary assembly and localization of IFT, BBS, and hedgehog components. X means that the process or localization was blocked by the mutation in the left column; = means that the process or localization is not affected by the mutation; and ↑ indicates that the protein is elevated in the cilia on the mutant cells. The crossed-out arrow means that we cannot detect the protein in cilia on wild-type cells and that the ciliary level is not increased in the mutant.

(B) Model for function of IFT25/IFT27. Details are provided in the Discussion.

Based on our data and on data in the literature, we developed the following model for IFT25/IFT27 function (Figure 7). Entry of Ptch1 and Smo into cilia appears to be independent of IFT25, IFT27, and the BBSome, as Ptch1 and Smo accumulate in cilia on *Ift25*, *Ift27*, *Bbs2*, and *Bbs7* mutant cells. Thus, our model focuses on the removal of these hedgehog components. IFT27 is a small G protein, and interactions of G proteins with other proteins are often regulated by the nucleotide bound to the G protein. The binding of IFT27 to IFT25 does not appear to depend on the type of guanine nucleotide bound, as the dimer formed as well with IFT27^{T19N} form (thought to mimic the GDP-bound or nucleotide-free state of IFT27) as it did with the IFT27^{K68L} (thought to reflect the GTP-bound state) and the wild-type forms. However, the IFT25/IFT27^{T19N} dimer was unable to associate with the rest of complex B when wild-type IFT27 was present, and the T19N mutant form was not able to fully rescue the Smo and BBS accumulation phenotypes of *Ift27* mutant cells. This suggests that, while IFT25/IFT27^{T19N} retains some ability to bind to the IFT particle, the affinity is reduced. The binding of IFT25/IFT27 to IFT complex B is likely through interactions with IFT81/IFT74 (Lucker et al., 2010; Bhogaraju et al., 2013).

IFT25/IFT27 could directly bind Smo, Ptch1, and Gpr161 to couple them to the IFT particle for removal from the cilium. However, in vitro Ptch1 and Smo accumulate in BBS-defective cilia, and the BBSome interacts directly with the cytoplasmic tail of Smo (Zhang et al., 2012). Our findings that the BBSome and Lztfl1 accumulate in *Ift27* mutant cilia, along with the data showing that the BBSome accumulates in *Lztfl1* mutant cilia, suggest that IFT25/IFT27 work with the BBSome through Lztfl1 to actively remove ciliary membrane proteins such as Ptch1, Smo, and Gpr161 in a signal-dependent manner. The relationship between Arl6 and IFT25/IFT27 remains to be established, but the observation that Arl6 accumulates in *Ift27* mutant cilia suggests that Arl6 requires IFT25/IFT27 for removal from cilia.

In addition to the role of IFT25/IFT27 in the regulated removal of Ptch1, Smo, and Gpr161 from cilia, IFT25/IFT27 may also play a role in transport of Gli2. *Ift25* and *Ift27* mutant cells fail to elevate Gli2 at the ciliary tip when the hedgehog pathway is activated. It is likely that this phenotype is largely indirect and due to the failure of the pathway to be activated. However, our SmoM2 results suggest that IFT25 and IFT27 do play a role in transporting Gli2 to the ciliary tip. When cells are transfected with this oncogenic form of Smo, the pathway downstream of Smo is activated. In wild-type cells, this causes accumulation of Gli2 at the ciliary tip, much like would be observed if the pathway were activated by ligand. In *Ift27* mutant cells transfected with SmoM2, the total amount of Gli2 in the cilia was similar to what was seen in control cells, but the protein was not concentrated at the tip as normally observed. This indicates that IFT25 and IFT27 are needed to transport Gli2 to the tip or the tip of *Ift27* mutant cilia that are abnormal. Live cell imaging will be needed to address this question.

Conclusions

In this work, we demonstrate that IFT27, like IFT25, is not required for ciliary assembly but is required for the dynamic movements of Ptch1, Smo, and Gpr161 that occur during hedgehog signaling. The BBSome and BBSome regulator Lztfl1 also accumulate in *Ift27* mutant cilia. This suggests a functional model whereby Lztfl1 coordinates the interactions between the

BBSome and the IFT particle to regulate the removal of Ptch1 and Smo from cilia at the appropriate times during hedgehog signaling.

EXPERIMENTAL PROCEDURES

Additional methods can be found in the Supplemental Experimental Procedures.

Mouse Breeding

Ift27$^{tm1a(EUCOMM)Hmgu}$-targeted embryonic stem cell line HEPD0653_7_E10 was obtained from the EUCOMM project and injected into C57Bl/6J albino blastocysts to generate chimeric animals. Chimeric mice were mated to C57Bl/6J albino mice [B6(Cg)-*Tyr*$^{c-2J}$/J, Jax 000058] or to C57Bl/6J mice (Jax 000664). This allele, *Ift27*^{neo}, was converted to *Ift27*^{null1}, *Ift27*^{flox}, and *Ift27*^{null2} using C57Bl/6 congenic PrmCre (O'Gorman et al., 1997) and FlpE (Farley et al., 2000) (Figure S1). In vivo *Gli1* expression was monitored using *Gli1-LacZ* (Jax 008211) (Bai et al., 2002). Genotyping was carried out as described in Figure S1. All mouse work was carried out at the University of Massachusetts Medical School (UMMS) and was approved by the UMMS Institutional Animal Care and Use Committee.

IF Microscopy

Cells for IF microscopy were grown, fixed, and stained as described elsewhere (Keady et al., 2012). Primary antibodies used included the following: acetylated tubulin (6-11B-1, Sigma), beta-tubulin (B-5-1-2, Sigma), gamma-tubulin (GTU-88, Sigma), MmIFT20, MmIFT52, MmIFT57, MmIFT88 (Pazour et al., 2005), MmIFT25 (Proteintech), MmIFT140 (Jonassen et al., 2012), Gli1 (V812, Cell Signaling), Gli3 (AF3690, R&D Systems), beta actin (13E5; Cell Signaling), Gli2 (a gift from J. Eggenschwiler, University of Georgia), Ptch1, Smo (gifts from R. Rohatgi, Stanford University), Dync2h1 (a gift from R. Vallee, Columbia University), Gpr161 (a gift from S. Mukhopadhyay, University of Texas Southwestern Medical Center), Arl6 (a gift from M. Nachury, Stanford University), BBS9 (Sigma and Proteintech), Lztfl1 and BBS5 (Proteintech), Pax6, Shh, and Olig2 (Developmental Studies Hybridoma Bank, University of Iowa). Anti-MmIFT25 and anti-MmSmo were made by expressing the mouse protein in bacteria as a maltose-binding protein fusion and injecting into rabbits (Figure S3). Antibodies were affinity purified against the same fragment expressed as a glutathione S-transferase fusion.

DNA Constructs

The following are DNA constructs used in this study.

Flag-GST (BK35): glutathione S-transferase from pGex6p1 cloned into JAF113 (Follit et al., 2009), a slightly modified p3xFLAG-myc-CMV-26 (Sigma) (Keady et al., 2011). TE24 is the equivalent construct in lentiviral vector pHAGE_DN_CMV_nucEGFP (a gift from D. Nedelcu and A. Salic).

Flag-GFP (JAF 146): EGFP cloned into JAF113.

Flag-IFT25 (JAF143): mouse *Ift25* cloned into JAF113. Flag-IFT25$^{T40R/T42R/S128E}$ (BK61) was made by PCR. TE14 and TE16 are equivalent constructs in the lentiviral vector pHAGE_DN_CMV_nucEGFP.

IFT27-Flag (BK8): mouse *Ift27* cloned into p3XFLAG-myc-CMV-14 (Sigma) (Follit et al., 2009). IFT27^{T19N}-Flag (BK12) and IFT27^{K68L}-Flag (BK10) were generated by PCR. TE17, TE19, and TE18 are equivalent constructs in pHAGE_DN_CMV_nucEGFP.

Flag-Lztfl1 (TE30): mouse *Lztfl1* cloned into pHAGE_DN_CMV_nucEGFP. Flag was added at the N terminus during PCR amplification.

Smo-M2-mCherry: SmoM2 in pHAGE_DN_CMV vector (a gift from D. Nedelcu and A. Salic).

CRISPR/Cas9 Genome Editing

Candidate single-guide RNAs were identified by searching for G(N)20GG motifs, 300 bases upstream and 100 bases downstream of the targeting sequence, that conform with the nucleotide requirements for U6 Pol III transcription and the spCas9 PAM recognition element (NGG) (Jinek et al., 2012; Mali et al., 2013) using the Web-based software ZiFiT targeter 4.2 (Sander et al., 2010). Sequences generated were aligned to mouse genome using nBLAST to search for potential off-target sites. Pairs of oligonucleotides were subsequently annealed together and cloned into pBSK-gRNA (a gift from R.Maehr). Finally, this construct was electroporated into NIH 3T3 cells, together with pCas9p2a (a gift from R. Maehr), and cells were selected for Cas9 vector expression with the appropriate antibiotic.

SUPPLEMENTAL INFORMATION

Supplemental Information includes Supplemental Experimental Procedures, five figures, four tables, and four movies and can be found with this article online at http://dx.doi.org/10.1016/j.devcel.2014.09.011.

ACKNOWLEDGMENTS

We thank Drs. S. Jones (Transgenic Mouse Core) and P. Furcinitti (Digital Imaging Core) for assistance during this work. We thank Dr. P. Odgren for use of his bright field microscope; and Drs. J. Eggenschwiler (Princeton University), R. Vallee (Columbia University), M. Nachury (Stanford University), R. Rohatgi (Stanford University), S. Mukhopadhyay (University of Texas Southwestern Medical Center), and S. Seo (University of Iowa) for reagents. We thank M. Nachury (Stanford University), B. Yoder (University of Alabama), Q. Zhang (University of Iowa), V. Sheffield (University of Iowa), L. Leehy, and R. Bortell (University of Massachussetts Medical School) for mouse fibroblasts. We thank Drs. D. Nedelcu and A. Salic (Harvard Medical School) for assistance with lentiviral constructs, Dr. R. Maher for assistance with genome editing, and Dr. E. Lorentzen for advice on IFT25/IFT27 structure. This work was supported by NIH grants GM060992 (to G.J.P.) and 5U01HL098180 (to C.W.L.) and funding from the European Community's Seventh Framework Programme FP7/2009 under grant agreement no. 241955 SYSCILIA to C.A.J. Y.L. was supported by a grant from the China Scholarship Council (no.2011621077). Z.A.A. was supported by a grant from the Rosetree's Trust (no. JS16/M279). Core resources supported by the Diabetes Endocrinology Research Center grant DK32520 and the Alabama Recessive Polycystic Kidney Disease Core Center DK074038 were used.

Received: June 11, 2014
Revised: September 12, 2014
Accepted: September 23, 2014
Published: October 30, 2014

REFERENCES

Aldahmesh, M.A., Li, Y., Alhashem, A., Anazi, S., Alkuraya, H., Hashem, M., Awaji, A.A., Sogaty, S., Alkharashi, A., Alzahrani, S., et al. (2014). IFT27, encoding a small GTPase component of IFT particles, is mutated in a consanguineous family with Bardet-Biedl syndrome. Hum. Mol. Genet. *23*, 3307–3315.

Badano, J.L., Mitsuma, N., Beales, P.L., and Katsanis, N. (2006). The ciliopathies: an emerging class of human genetic disorders. Annu. Rev. Genomics Hum. Genet. *7*, 125–148.

Bai, C.B., Auerbach, W., Lee, J.S., Stephen, D., and Joyner, A.L. (2002). Gli2, but not Gli1, is required for initial Shh signaling and ectopic activation of the Shh pathway. Development *129*, 4753–4761.

Berbari, N.F., Lewis, J.S., Bishop, G.A., Askwith, C.C., and Mykytyn, K. (2008). Bardet-Biedl syndrome proteins are required for the localization of G protein-coupled receptors to primary cilia. Proc. Natl. Acad. Sci. USA *105*, 4242–4246.

Bhogaraju, S., Taschner, M., Morawetz, M., Basquin, C., and Lorentzen, E. (2011). Crystal structure of the intraflagellar transport complex 25/27. EMBO J. *30*, 1907–1918.

Bhogaraju, S., Cajanek, L., Fort, C., Blisnick, T., Weber, K., Taschner, M., Mizuno, N., Lamla, S., Bastin, P., Nigg, E.A., and Lorentzen, E. (2013). Molecular basis of tubulin transport within the cilium by IFT74 and IFT81. Science *341*, 1009–1012.

Chen, J.K., Taipale, J., Young, K.E., Maiti, T., and Beachy, P.A. (2002). Small molecule modulation of Smoothened activity. Proc. Natl. Acad. Sci. USA *99*, 14071–14076.

Cole, D.G., Diener, D.R., Himelblau, A.L., Beech, P.L., Fuster, J.C., and Rosenbaum, J.L. (1998). *Chlamydomonas* kinesin-II-dependent intraflagellar

transport (IFT): IFT particles contain proteins required for ciliary assembly in *Caenorhabditis elegans* sensory neurons. J. Cell Biol. *141*, 993–1008.

Cong, L., Ran, F.A., Cox, D., Lin, S., Barretto, R., Habib, N., Hsu, P.D., Wu, X., Jiang, W., Marraffini, L.A., and Zhang, F. (2013). Multiplex genome engineering using CRISPR/Cas systems. Science *339*, 819–823.

Farley, F.W., Soriano, P., Steffen, L.S., and Dymecki, S.M. (2000). Widespread recombinase expression using FLPeR (flipper) mice. Genesis *28*, 106–110.

Follit, J.A., Xu, F., Keady, B.T., and Pazour, G.J. (2009). Characterization of mouse IFT complex B. Cell Motil. Cytoskeleton *66*, 457–468.

Haycraft, C.J., Banizs, B., Aydin-Son, Y., Zhang, Q., Michaud, E.J., and Yoder, B.K. (2005). Gli2 and Gli3 localize to cilia and require the intraflagellar transport protein polaris for processing and function. PLoS Genet. *1*, e53.

Huangfu, D., Liu, A., Rakeman, A.S., Murcia, N.S., Niswander, L., and Anderson, K.V. (2003). Hedgehog signalling in the mouse requires intraflagellar transport proteins. Nature *426*, 83–87.

Huet, D., Blisnick, T., Perrot, S., and Bastin, P. (2014). The GTPase IFT27 is involved in both anterograde and retrograde intraflagellar transport. eLife *3*, e02419.

Iomini, C., Li, L., Esparza, J.M., and Dutcher, S.K. (2009). Retrograde intraflagellar transport mutants identify complex A proteins with multiple genetic interactions in Chlamydomonas reinhardtii. Genetics *183*, 885–896.

Jin, H., White, S.R., Shida, T., Schulz, S., Aguiar, M., Gygi, S.P., Bazan, J.F., and Nachury, M.V. (2010). The conserved Bardet-Biedl syndrome proteins assemble a coat that traffics membrane proteins to cilia. Cell *141*, 1208–1219.

Jinek, M., Chylinski, K., Fonfara, I., Hauer, M., Doudna, J.A., and Charpentier, E. (2012). A programmable dual-RNA-guided DNA endonuclease in adaptive bacterial immunity. Science *337*, 816–821.

Jonassen, J.A., SanAgustin, J., Baker, S.P., and Pazour, G.J. (2012). Disruption of IFT complex A causes cystic kidneys without mitotic spindle misorientation. J. Am. Soc. Nephrol. *23*, 641–651.

Keady, B.T., Le, Y.Z., and Pazour, G.J. (2011). IFT20 is required for opsin trafficking and photoreceptor outer segment development. Mol. Biol. Cell *22*, 921–930.

Keady, B.T., Samtani, R., Tobita, K., Tsuchya, M., San Agustin, J.T., Follit, J.A., Jonassen, J.A., Subramanian, R., Lo, C.W., and Pazour, G.J. (2012). IFT25 links the signal-dependent movement of Hedgehog components to intraflagellar transport. Dev. Cell *22*, 940–951.

Ko, H.W., Liu, A., and Eggenschwiler, J.T. (2009). Analysis of hedgehog signaling in mouse intraflagellar transport mutants. Methods Cell Biol. *93*, 347–369.

Lechtreck, K.F., Johnson, E.C., Sakai, T., Cochran, D., Ballif, B.A., Rush, J., Pazour, G.J., Ikebe, M., and Witman, G.B. (2009). The Chlamydomonas reinhardtii BBSome is an IFT cargo required for export of specific signaling proteins from flagella. J. Cell Biol. *187*, 1117–1132.

Lucker, B.F., Miller, M.S., Dziedzic, S.A., Blackmarr, P.T., and Cole, D.G. (2010). Direct interactions of intraflagellar transport complex B proteins IFT88, IFT52, and IFT46. J. Biol. Chem. *285*, 21508–21518.

Mali, P., Yang, L., Esvelt, K.M., Aach, J., Guell, M., DiCarlo, J.E., Norville, J.E., and Church, G.M. (2013). RNA-guided human genome engineering via Cas9. Science *339*, 823–826.

Mukhopadhyay, S., Wen, X., Ratti, N., Loktev, A., Rangell, L., Scales, S.J., and Jackson, P.K. (2013). The ciliary G-protein-coupled receptor Gpr161 negatively regulates the Sonic hedgehog pathway via cAMP signaling. Cell *152*, 210–223.

O'Gorman, S., Dagenais, N.A., Qian, M., and Marchuk, Y. (1997). Protomine-Cre recombinase transgenes efficiently recombine target sequences in the male germ line of mice, but not in embryonic stem cells. Proc. Nat. Acad. Sci. USA *94*, 14602–14607.

Ou, G., Koga, M., Blacque, O.E., Murayama, T., Ohshima, Y., Schafer, J.C., Li, C., Yoder, B.K., Leroux, M.R., and Scholey, J.M. (2007). Sensory ciliogenesis in *Caenorhabditis elegans*: assignment of IFT components into distinct modules based on transport and phenotypic profiles. Mol. Biol. Cell *18*, 1554–1569.

Pazour, G.J., Agrin, N., Leszyk, J., and Witman, G.B. (2005). Proteomic analysis of a eukaryotic cilium. J. Cell Biol. *170*, 103–113.

Pedersen, L.B., and Rosenbaum, J.L. (2008). Intraflagellar transport (IFT) role in ciliary assembly, resorption and signalling. Curr. Top. Dev. Biol. *85*, 23–61.

Qin, H., Wang, Z., Diener, D., and Rosenbaum, J. (2007). Intraflagellar transport protein 27 is a small G protein involved in cell-cycle control. Curr. Biol. *17*, 193–202.

Rosenbaum, J.L., and Witman, G.B. (2002). Intraflagellar transport. Nat. Rev. Mol. Cell Biol. *3*, 813–825.

Sander, J.D., Maeder, M.L., Reyon, D., Voytas, D.F., Joung, J.K., and Dobbs, D. (2010). ZiFiT (Zinc Finger Targeter): an updated zinc finger engineering tool. Nucleic Acids Res. *38*, W462–W468.

Satir, P., and Christensen, S.T. (2007). Overview of structure and function of mammalian cilia. Annu. Rev. Physiol. *69*, 377–400.

Seo, S., Zhang, Q., Bugge, K., Breslow, D.K., Searby, C.C., Nachury, M.V., and Sheffield, V.C. (2011). A novel protein LZTFL1 regulates ciliary trafficking of the BBSome and Smoothened. PLoS Genet. *7*, e1002358.

Xie, J., Murone, M., Luoh, S.M., Ryan, A., Gu, Q., Zhang, C., Bonifas, J.M., Lam, C.W., Hynes, M., Goddard, A., et al. (1998). Activating Smoothened mutations in sporadic basal-cell carcinoma. Nature *391*, 90–92.

Zhang, Q., Seo, S., Bugge, K., Stone, E.M., and Sheffield, V.C. (2012). BBS proteins interact genetically with the IFT pathway to influence SHH-related phenotypes. Hum. Mol. Genet. *21*, 1945–1953.